Radial-Flux Permanent-Magnet Hub Drives: A Comparison Based on Stator and Rotor Topologies

Arnold J. Rix, *Member, IEEE*, and Maarten J. Kamper, *Senior Member, IEEE*

***Abstract*—In this paper, the performances of electric vehicle (EV) in-wheel (hub) nonoverlap-winding permanent-magnet motors with different stator and rotor topologies are compared. The calculation of the frequency losses in the design optimization of the hub motors is specifically considered. Also, the effect of the slot and pole number choice that determines the winding factor of the machine is investigated. It is shown that the torque-per-copper-loss performance of the machine cannot be judged solely on the winding factor of the machine. Wide open stator slot machines with rectangular preformed coils and, hence, low manufacturing costs are found to perform better than expected. The design detail and test results of a prototype 10-kW water-cooled EV hub drive are presented. The test results confirm the finite-element-calculated results, specifically in the high-speed region of the drive where the rotor topology affects the constant power speed range.**

***Index Terms*—Concentrated winding, design optimization, electric vehicle (EV), hub drive, in-wheel, losses, permanent magnet (PM), prototype manufacturing, radial flux.**

NOMENCLATURE

α	Loss constant.
B	Flux density amplitude (in teslas).
b_c	Coil width (in millimeters).
b_m	Magnet width (in millimeters).
d	Diameter of conductor (in meters).
d_g	Air-gap diameter (in millimeters).
ϕ	Current angle (in electrical degrees).
F	Objective function.
f	Electrical frequency (in hertz).
h_c	Coil height (in millimeters).
h_m	Magnet height (in millimeters).
I_d	d-axis current (in amperes).
I_q	q-axis current (in amperes).
J	Current density (in amperes per square millimeter).
$J_{\max}$	Maximum current density (in amperes per square millimeter).
k_d	Distribution factor.
k_e	Eddy current loss coefficient.
k_{exc}	Excess loss coefficient.
k_h	Hysteresis loss coefficient.
k_p	Pitch factor.
k_w	Winding factor.
l	Active length of conductor (in meters).
λ_d	d-axis flux linkage (in weber turns).
λ_q	q-axis flux linkage (in weber turns).
λ_{PM}	Permanent-magnet (PM) flux linkage (in weber turns).
L_d	d-axis inductance (in henrys).
L_q	q-axis inductance (in henrys).
m_j	Mass of region j (in kilograms).
n_{cj}	Number of stator conductors in region j.
p	Number of poles.
P_c	Iron core losses (in watts).
P_f	Frequency losses (in watts).
P_m	PM losses (in watts).
P_s	Stator conductor eddy current losses (in watts).
p_c	Iron core losses (in watts per kilogram).
p_e	Iron eddy current losses (in watts per kilogram).
p_{exc}	Excess specific loss (in watts per kilogram).
p_h	Iron hysteresis losses (in watts per kilogram).
T	Torque (in newton meters).
T_{ave}	Average torque (in newton meters).
T_{ripple}	Torque ripple (in percent).
Vol_j	Volume of region j (in cubic meters).
w	Weighting factor.
ε	Error function.
ρ	Resistivity of copper (in ohm meters).

Manuscript received December 17, 2010; revised March 25, 2011 and June 19, 2011; accepted June 26, 2011. Date of publication July 14, 2011; date of current version February 10, 2012.

A. J. Rix is with Isivunguvungu Wind Energy Converter (Pty) Ltd., Cape Town 8000, South Africa (e-mail: rix@afrihost.co.za).

M. J. Kamper is with the Department of Electrical and Electronic Engineering, Stellenbosch University, Stellenbosch 7600, South Africa (e-mail: kamper@sun.ac.za).

Color versions of one or more of the figures in this paper are available online at http://ieeexplore.ieee.org.

Digital Object Identifier 10.1109/TIE.2011.2161654

I. INTRODUCTION

HYBRID electric vehicles (EVs) and EVs have received wide interest lately and are considered as the next generation of vehicles for passenger transport [1]–[6]. Furthermore, in-wheel (hub) motor drives are considered as possible drive trains for EVs. The use of EV hub drives allows for better vehicle control and opens the possibility for higher system efficiency due to the exclusion of gearboxes. However, important disadvantages of hub motor drives do exist, which include system cost and higher unsprung mass [7].

The per-wheel torque and power performance that is required of a typical 1600-cm^3 internal combustion engine (ICE)-powered vehicle to maintain a constant speed is shown in Fig. 1. The torque and power at each wheel are calculated from vehicle models as given in [8], assuming a four-wheel drive vehicle. Also shown in Fig. 1 are the torque and power per wheel of a gearless PM hub drive motor. Interesting from Fig. 1 are the

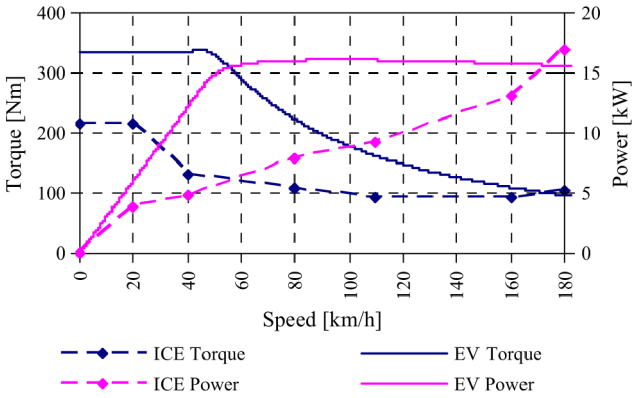

Fig. 1. ICE-powered wheel torque and wheel power required to maintain a constant speed and EV hub motor wheel torque and power versus vehicle speed.

typical required rated torque and rated power per wheel of the EV hub motor, namely, 300–400 N · m and 15–20 kW.

The torque and power performance of the EV hub motor drive in Fig. 1 is that of a nonoverlapping concentrated-coil radial-flux PM machine. This is the type of PM machine investigated in this paper for EV hub motor applications. The technology of these PM machines, among others, reduces manufacturing cost [9], increases efficiency by reducing end winding length [10], [11], and exhibits high torque quality [12]. Various possible pole–slot combinations can be used for the concentrated-coil PM machine [13]–[15]. The final pole-slot choice is influenced by the possible vibrations and noise of the machine due to unbalanced magnetic forces and torque ripple [11], [16]–[18]. The machine losses are also affected by the pole-slot choice as explained in [19].

The winding factors for the different pole-slot combinations are explained and given in [13] and [20]. Normally, PM machines with high winding factors are considered as the best machines.

Axial-flux PM hub motors for EVs have received some attention in the literature, but little has been published on radial-flux PM machines for this application. Also lacking in the literature are published performance data of EV hub drives. In this paper, a complete performance evaluation of optimally designed radial-flux PM hub motors with different design configurations is presented. This evaluation includes a performance comparison between low-winding-factor machines and good-winding-factor machines, an aspect that is also lacking in the literature.

A prototype 10-kW water-cooled PM hub drive has been designed, built, and tested to verify the results obtained from finite-element (FE) analysis (FEA) and to explore the impact on manufacturability of straight stator teeth and open slots combined with preformed coils.

II. Design Aspects

The important stator and rotor design aspects and design parameters of the nonoverlap-winding PM hub machine are considered in this section. These design aspects and parameters are dealt with in the following sections.

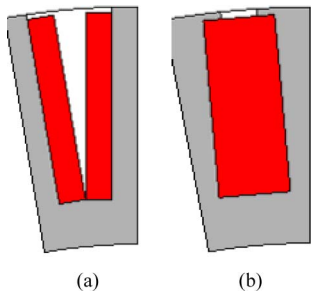

Fig. 2. Stator design options. (a) Open slot. (b) Semiclosed slot.

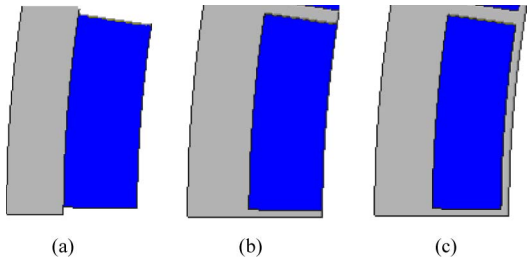

Fig. 3. Rotor design options. (a) Surface PM. (b) Embedded PM. (c) Interior PM.

A. Pole-Slot Combination

A substantial amount of work has been published on the winding factors of various pole-slot combinations of concentrated-coil PM machines [13], [14], [21], [22]. A high winding factor is seen as a prerequisite and main criterion in the choice of a pole-slot combination for an iron-cored nonoverlap-winding PM machine. The winding factor given by

$$k_w = k_d k_p \tag{1}$$

and derived and described in [20] consists of the product of the distribution factor k_d and the pitch factor k_p.

Considering the works done in [16] and [23], a pole-slot combination that gives the highest lcm value and a gcd value of greater than unity should be chosen; a high lcm value indicates a lower torque ripple, while a low gcd value is congruent with a high winding factor.

B. Stator Slot Shape

The stator slot shapes investigated for the EV hub motor application are divided into open- and semiclosed-slot shapes, as shown in Fig. 2(a) and (b), respectively. A comparison of these two types of slots in the performance of brushless dc machines is also done in [24], although for a different application. Only double-layer nonoverlap windings are considered in the comparison study.

C. Rotor Configuration

A few rotor design options that affect specifically the torque and constant power speed range (CPSR) performance of the PM machine are investigated in this paper. The rotor design options include surface-mounted, embedded, and interior magnets, as shown in Fig. 3(a)–(c), respectively.

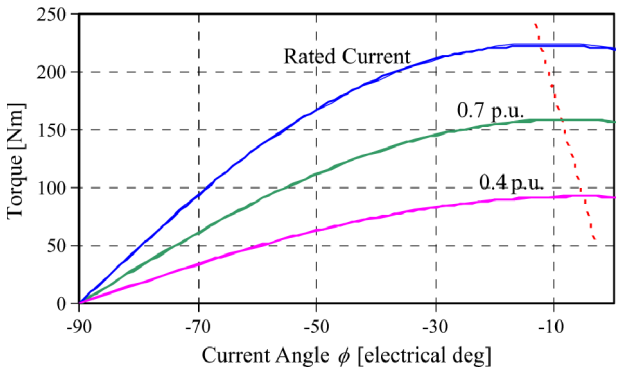

Fig. 4. Torque versus current angle with per-unit current as parameter.

D. Current Angle

The torque can be calculated using dq flux linkages and currents of the dq-axis equivalent circuits as

$$T = \frac{3}{4}p(\lambda_d I_q - \lambda_q I_d) = \frac{3}{4}p\lambda_{\mathrm{PM}} I\cos(\phi) + \frac{3}{8}p(L_d - L_q)I^2\sin(2\phi) \quad (2)$$

where λ is the flux linkage, L is the corresponding inductance, and ϕ is the current angle. The torque equation in (2) expresses the torque as a function of the current angle ϕ which is a drive control parameter. The torque versus current angle of a concentrated-coil radial-flux PM hub drive with interior PMs is shown, e.g., in Fig. 4, with the optimum current angle at rated speed indicated by the dotted line. As the speed increases into the constant power speed region, the current angle needs to be advanced in order to weaken the resultant flux.

III. FE Design Optimization

The FE modeling and performance calculation of the concentrated-coil PM machine described in Section II, together with Powell's nongradient optimization algorithm [25], is used to optimize the design of the machine; this method and the process used are very much the same as described in [26].

In the design software, with each iteration, the optimization algorithm calls the FE program to calculate the performance of the machine and the objective function value according to certain given machine dimensions and conditions. The FE program then remeshes the machine topology, solves for the magnetic vector potentials, and calculates the machine performance; this calculation includes the position step of the machine to determine the torque ripple and efficiency of the machine. The calculated performance and objective function value are then fed back to the optimization algorithm to be used in the next optimization iteration. The design optimization, thus, varies the dimensions and control parameters of the machine to obtain the best possible machine performance within the specified design limitations.

A. Objective Function

As the different stator and rotor design options and configurations as described in Section II result in very different performances in the high-speed region of the machine, the design optimization is done at the base speed rather than at the maximum speed of the PM machine drive. In terms of Fig. 1, thus, the best possible machine performance is needed at 50-km/h vehicle speed and not, e.g., at 180 km/h. The high-speed performance, specifically the CPSR, of the PM machine drive is then studied as a result of the design optimization done at the base speed.

The design optimization at the base speed is done by maximizing the torque per I^2R copper loss of the machine subject to certain design constraints. In this way, the torque-per-copper-loss performance of the PM machines can be compared, which is important in the low-speed region of the machines. The other machine performances like torque ripple, torque per active mass, and efficiency are studied and compared as a result of the torque-per-copper-loss design optimization.

For the particular hub drive EV case studied, the I^2R copper loss of the PM machines is set at a rated value of 1 kW, in accordance with the cooling and thermal model, in the FE program and used in the design optimization. The objective function to be maximized only includes the average torque T_{ave} of the machine calculated by the FE program. The only constraint applied in the design optimization is a constraint on the current density J, namely, that $J \leq J_{\max}$. The constraint optimization is done by modifying the objective function by adding a weighting penalty function that assigns a positive penalty for increased constraint violation. The objective function, hence, is defined as

$$F = T_{\mathrm{ave}} - w\varepsilon \quad (3)$$

where

$$\varepsilon = \begin{cases} (J - J_{\max})^2 & : J > J_{\max} \\ 0 & : J \leq J_{\max} \end{cases} \quad (4)$$

and w is an associated weighting factor.

After the design optimization, the number of turns in series per phase of the winding of the particular PM machine is adjusted so that the machine complies with the voltage limit at the base speed.

B. Optimization Parameters

The machine parameters that are kept constant in the optimization procedure are the copper losses (P_{cu}), current angle (ϕ), outer diameter, inner diameter, and stack length of the machine. By keeping the outer machine dimensions constant, the active volume of the machine is kept constant. This is a prerequisite for the mechanical design and the support structure that needs to fit inside a standard-size wheel rim. The five machine dimensions that are varied and optimized in the design, to maximize (3), are the air-gap diameter (d_g), coil width (b_c), coil height (h_c), magnet pitch (b_m), and magnet height (h_m), as shown in Fig. 5.

C. Frequency Loss and Torque Ripple Calculations

In addition to the I^2R copper losses, the calculation of the iron and eddy current losses in the machine, defined as

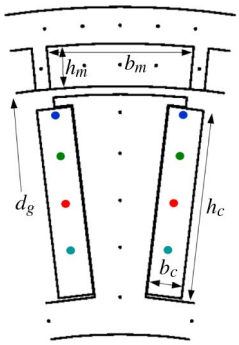

Fig. 5. Region points in a PM machine section.

TABLE I
40-POLE/30-SLOT OPTIMIZATION RESULTS PER 1-kW I^2R LOSS

Slot type	Semi-closed slots		
Magnets	Surface	Embedded	Interior
k_w/ LCM / GCD	0.866 / 120 / 10		
b_m [mm]	17.8	17.8	17.7
h_m [mm]	7.2	7.0	6.6
T_{ave} [Nm]	339.7	336.2	294.7
T_{ave}/Mass [Nm/kg]	18.95	18.5	16.21
T_{ripple} [%]	28.7	18.2	9.6
CPSR	1.9	5.2	5.37
Efficiency [%]	91.8	91.8	91.7
Slot type	Open slots		
Magnets	Surface	Embedded	Interior
k_w/ LCM / GCD	0.866 / 120 / 10		
b_m [mm]	17.8	17.8	17.6
h_m [mm]	6.1	6.3	5.7
T_{ave} [Nm]	308.7	310.1	281.3
T_{ave}/Mass [Nm/kg]	18.93	18.81	17.05
T_{ripple} [%]	11.7	21.6	24.2
CPSR	1.6	2.05	4.7
Efficiency [%]	88.2	88.8	89.5

frequency losses P_f, is important. These losses consist of the stator and rotor iron core losses P_c, the eddy current losses in the stator conductors P_s, and the eddy current losses in the PMs P_m, i.e.,

$$P_f = P_c + P_s + P_m. \tag{5}$$

The method applied to calculate the frequency losses in (5) is explained in the Appendix, with the specific loss component equations also given. These loss calculations are done after the design optimization of the machines and used to calculate the efficiencies of the machines.

The peak-to-peak torque is expressed as a percentage of the average torque and called torque ripple. The torque ripple values obtained for the different machines are given in Tables I and II. Cogging torque is the peak-to-peak torque, at no load, expressed as a percentage of the average torque. A hub motor will rarely be operated under no-load conditions, so specific attention was not given to this subject. If cogging torque would be a problem, the magnet width could be adjusted slightly to minimize the cogging torque without having a great impact on the average torque.

TABLE II
40-POLE/36-SLOT OPTIMIZATION RESULTS PER 1-kW I^2R LOSS

Slot type	Semi-closed slots		
Magnets	Surface	Embedded	Interior
k_w/ LCM / GCD	0.945 / 360 / 4		
b_m [mm]	17.7	17.7	17.7
h_m [mm]	7.6	7.6	7.4
T_{ave} [Nm]	337.3	326.6	290.2
T_{ave}/Mass [Nm/kg]	18.94	18.06	16.04
T_{ripple} [%]	4.0	4.5	2.1
CPSR	1.3	1.85	5.9
Efficiency [%]	93.9	93.7	93.4
Slot type	Open slots		
Magnets	Surface	Embedded	Interior
k_w/ LCM / GCD	0.945 / 360 / 4		
b_m [mm]	17.8	17.8	17.8
h_m [mm]	6.2	7.0	6.0
T_{ave} [Nm]	304.1	303.5	275.3
T_{ave}/Mass [Nm/kg]	18.39	17.97	16.43
T_{ripple} [%]	1.0	2.1	2.1
CPSR	1.3	1.45	2.05
Efficiency [%]	89.8	90.6	91.5

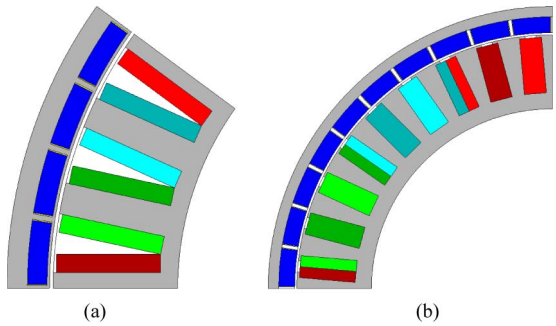

Fig. 6. FE machine models used in the design optimization. (a) 30-slot machine. (b) 36-slot machine.

IV. DESIGN OPTIMIZATION RESULTS

The design optimizations are performed to investigate the effect of the various stator and rotor designs and slot–pole combinations discussed in Section II. The pole-slot combinations investigated are a 40-pole/30-slot machine with a winding factor of 0.866 and a 40-pole/36-slot machine with a winding factor of 0.945. The 30-slot stator is specifically chosen to investigate a machine with a low winding factor. The pole number of both machines is fixed to keep the machine speed and frequency the same so that losses can be compared on an equal basis. Fig. 6(a) shows a machine section (one-tenth) of the 40-pole/30-slot machine with open slots and interior magnets, while Fig. 6(b) shows a section (one-fourth) of the 40-pole/36-slot machine with surface-mounted magnets and semiclosed slots.

A. Torque and Efficiency Comparison

From the design optimization results in Tables I and II, it is clear that the winding factor is not an accurate indication of the torque-per-copper-loss performance of the machine. In fact, the low-winding-factor PM machines are found to have a higher torque-per-copper-loss performance than the good-winding-factor PM machines. The efficiency, however, of the

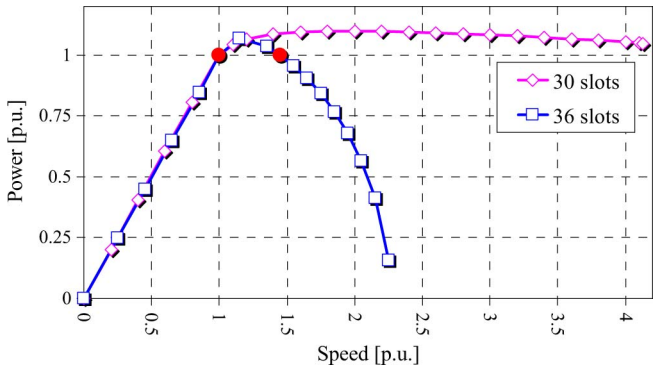

Fig. 7. Rated-power-versus-speed curves of 40-pole/30-slot and 40-pole/36-slot PM hub machines.

low-winding-factor machines is typically 2% lower than that of the good-winding-factor machines. As the I^2R copper loss of all the machines is the same, low-winding-factor machines are shown to have higher iron and magnet losses, i.e., for a given pole number.

Other factors, such as the slot and rotor topologies, have a large effect on the machine performance. The open-slot PM machines have 5%–10% less torque per copper loss than the semiclosed-slot PM machines. However, the active mass of the open-slot machines is less, so the torques per active mass of the open- and semiclosed-slot PM machines are very much the same.

If, thus, only these results are considered, the open-slot machines have the advantage of a lower manufacturing cost due to the use of preformed stator coils.

The lcm value of the 40-pole/36-slot machines is three times higher than that of the 40-pole/30-slot machines. Although the relationship between the lcm value and the torque ripple is not linear, it gives a clear indication of the torque quality of the machine. The lcm value is also an indication of the losses of a machine relative to another machine with the same pole number.

B. CPSR

The CPSR is defined as the ratio of the highest speed to the base speed of the hub motor for which the power output of the machine is equal to 1 p.u. These power points are indicated, e.g., on the power curve in Fig. 7 by the dots at 1-p.u. power. Note that, for the 40-pole/30-slot machine, there is only one dot, indicating that this machine has a CPSR of greater than the maximum speed shown on the x-axis. The CPSR as indicated in Table I of the 40-pole/30-slot machine with semiclosed stator slots and embedded magnets is equal to 5.2. The difference in the CPSRs of the two machines in Fig. 7 can be attributed to a 20% difference in the d-axis inductance of these machines. From Tables I and II, it can be seen that surface-mounted PM machines have lower CPSRs compared to the embedded and interior-mounted PM rotor machines.

V. Measured Results

A. Prototype Manufacturing

A small 10-kW 40-pole/30-slot water-cooled EV hub PM machine with an interior PM rotor was built and tested to confirm the FE results [26]. Due to the high current density of almost 10 A/m^2, the mechanical design included a water cooling system for the stator.

(a) (b)

Fig. 8. Prototype 10-kW 40-pole/30-slot stator and PM rotor. (a) Stator laminations and windings. (b) Rotor laminations and magnets.

(a) (b)

Fig. 9. Prototype 10-kW 40-pole/30-slot stator manufacturing. (a) Removing the stator mold. (b) Finished stator.

Fig. 10. Prototype 10-kW 40-pole/30-slot concentrated-coil EV PM hub motor with open slots and interior PM rotor.

The stator laminations and phase windings can be seen in Fig. 8(a). The stator laminations are press fit on the aluminum stator inner to help increase the thermal conductivity of this junction. Rectangular wire is used to improve the filling factor and, thus, increase the current-carrying ability of the phase winding. The practical fill factor obtained was equal to 0.59. From Fig. 8(a), it can be seen that it is easy to assemble the coils on the stator that has straight teeth and open slots. Epoxy resin is used to encapsulate the active material of the stator to help secure the windings and to serve as further insulation and protection against vibration. The stator is removed from the mold after the epoxy has cured, as shown in Fig. 9(a). The completed stator is shown in Fig. 9(b).

Part of the completed rotor is shown in Fig. 8(b). The rotor configuration makes assembly very easy and reduces assembly time, with the benefit of secure magnets. The assembled machine complete with an internal position sensor and a tire is shown in Fig. 10.

TABLE III
OPTIMIZED MACHINE SPECIFICATIONS

	10 kW Prototype	17 kW Design
Poles	40	
Slots	30	36
Rotor design	Interior PMs	
Rotor OD [mm]	270	
Rotor ID [mm]	248.99	246.48
Rotor yoke height [mm]	4.22	5.11
Magnet height (h_m) [mm]	5.54	5.9
Magnet pitch (b_m) [p.u.]	7/9	9/10
Magnet type	NdFeB	
Stator design	Open slots	
Stator OD [mm]	246.99	244.48
Stator ID [mm]	172	172
Stator yoke height [mm]	4.88	7.12
Tooth width [mm]	6.72	7.25
Coil width (b_c) [mm]	6.17	4.49
Coil height (h_c) [mm]	31.62	28.12
Active length [mm]	80	100

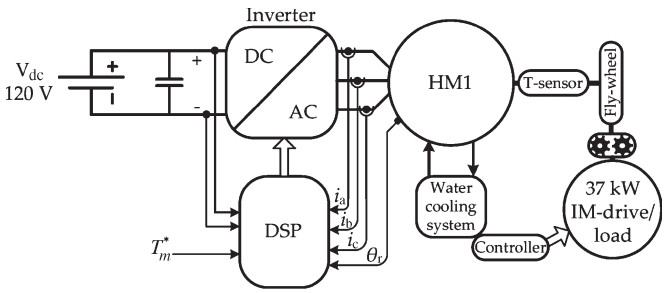

Fig. 11. Test setup diagram for (HM1) the prototype hub motor.

B. Measured Results

The rotor and stator dimensions of the 10-kW prototype are given in Table III, together with the dimensions of an optimized design from Table III. The 10-kW machine is connected via a torque sensor to a flywheel, which, in turn, is connected to a 37-kW induction machine that is used as drive and load, as shown in Fig. 11. The flywheel is used to filter the torque produced by the induction machine and enable a better reading of the PM machine's torque. The gearbox shown in Fig. 11, with a gear ratio of 1 : 3, is used to step up the speed of the hub motor to match the speed characteristics of the induction machine drive better.

The 10-kW prototype's torque and speed are controlled via a TMS 320 VC 33 digital signal processor and an inverter. The power electronic drive consists of a three-phase half-bridge inverter using 200-A insulated-gate bipolar transistor modules and is supplied by a lead acid battery pack with a nominal voltage of 120 V. Part of this laboratory setup is shown in Fig. 12, with the various components indicated as such. All six terminals of the three-phase windings of the hub motor are made available, and for testing, the water-cooled hub motor is connected in a Y configuration. A unique control algorithm described in [27] is implemented and used to control the PM machine throughout the entire speed range.

To confirm the results from the FEA, the open-circuit voltage and torque under load conditions are tested. The open-circuit

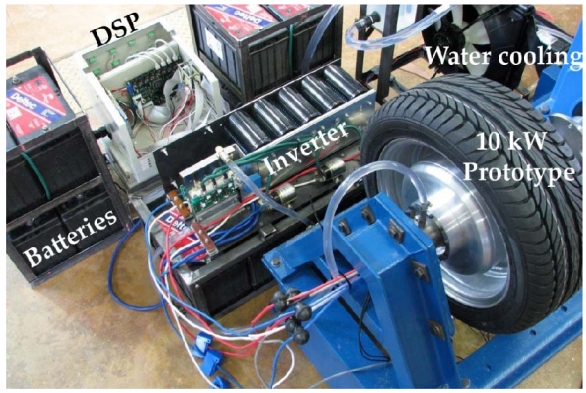

Fig. 12. Prototype PM hub motor drive under bench testing.

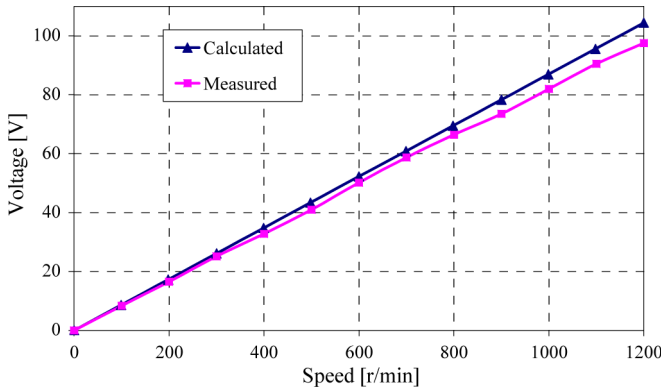

Fig. 13. Measured and calculated peak-to-peak phase voltages of the prototype PM hub motor throughout the entire speed range.

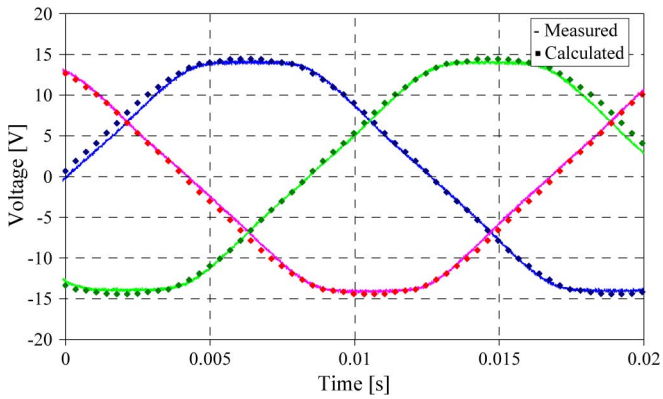

Fig. 14. Measured and calculated phase voltages of the prototype PM hub motor measured at 120 r/min.

voltage of the prototype 120-V dc-bus PM EV hub drive is shown in Figs. 13 and 14. The calculated and measured open-circuit voltages of the machine in Fig. 13 show good correlation, with the difference being less than 10%. This difference is due to the actual magnet size being smaller than that used in the FEA. This was corrected and with excellent comparative results shown in Fig. 14.

Loading of the machine was first tested at low speed in generator and motor modes. These tests consist of changing the current angle given fixed current amplitudes. Fig. 15 shows the results of the load test with the solid line being the FE-predicted values and the measured values indicated by the markers.

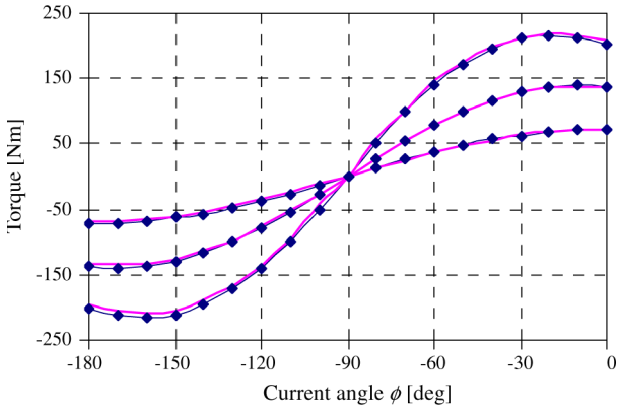

Fig. 15. Measured and calculated torques versus current angle at one-third, two-third, and full load currents of the PM hub drive (measured values are indicated with markers).

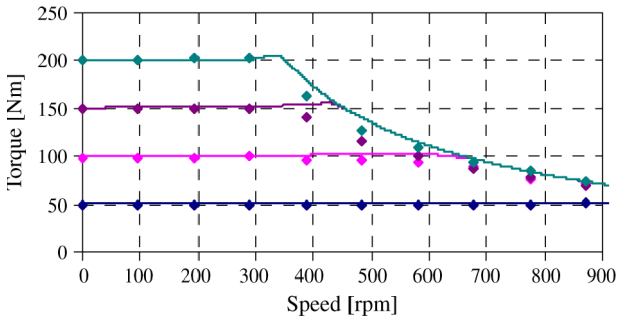

Fig. 16. Measured and calculated torques versus speed at 0.25-, 0.5-, 0.75-, and 1.0-p.u. currents of the PM hub drive (measured values are indicated with markers).

Next, the machine performance through the whole speed range was tested, with the correlation with the FE results shown in Fig. 16. This shows that the PM hub machine achieves the predicted maximum speed under the given load conditions and, thus, confirms the CPSR calculations. These results confirm, at least to a certain extent, the optimization performance results of the machines described in this paper.

After testing, the prototype PM hub motor was installed on a small utility vehicle for some testing, as shown in Fig. 17. Extensive modifications had to be made to the standard vehicle to accommodate the hub motor that is used as a rear wheel drive in this case.

VI. Conclusion

In this paper, the performance of 12 different optimum designed double-layer PM concentrated-coil machines for EV hub drive applications has been considered. Moreover, the practical design detail and test results of a developed low-cost water-cooled PM hub drive for an EV have been presented. From the study, the following conclusions are drawn.

1) It is shown that the torque-per-copper-loss performance of concentrated-coil PM machines cannot be judged solely on the winding factors of these machines. Furthermore, although the developed torque-per-copper-loss performance of PM machines with wide open stator slots is found to be 5%–10% less than that of PM machines with semiclosed stator slots, the torque per active mass is found to be the same for these machines.
2) The rotor iron losses are significant compared to the stator iron losses and must be considered in concentrated-coil machine designs. The PM machines with low winding factors and low lcm values have higher iron and magnet losses, and thus lower efficiencies, than machines with good winding factors and higher lcm values. Furthermore, there is a clear tendency that machines with wide open slots and rectangular coil shapes have higher iron, magnet, and stator eddy current losses than machines with semiclosed stator slots. However, this loss difference is found to be less in machines with good winding factors than in machines with relatively low winding factors.
3) As is generally known, the rotor topology severely affects the average torque and CPSR of the concentrated-coil PM machine. Machines with interior PM rotors are shown to have 9%–14% less developed torque-per-copper-loss performance than machines with surface-mounted PM rotors; however, these machines have a much better CPSR.
4) An important general finding is that the performance of wide open stator slot machines with rectangular preformed coils and, thus, low manufacturing costs is surprisingly better than what was expected. This is particularly the case for machines with good winding factors.
5) The stator and rotor topologies of the prototype PM hub motor investigated in this paper are expected to reduce manufacturing time and, hence, the total manufacturing cost. This radial-flux PM motor is practically shown to be a viable option as an EV hub motor.

Fig. 17. Prototype 10-kW 40-pole/30-slot in-wheel PM hub motor installed on a small utility vehicle for testing.

Appendix

To calculate the frequency losses accurately, the machine is divided into small regions where the harmonic flux density components are determined from time stepping FEA. This is done by determining the flux density harmonic components at the center (middle) points of the regions in the machine and then assuming each center point flux density as the flux density of that region. An example of the center region points is shown in Fig. 5.

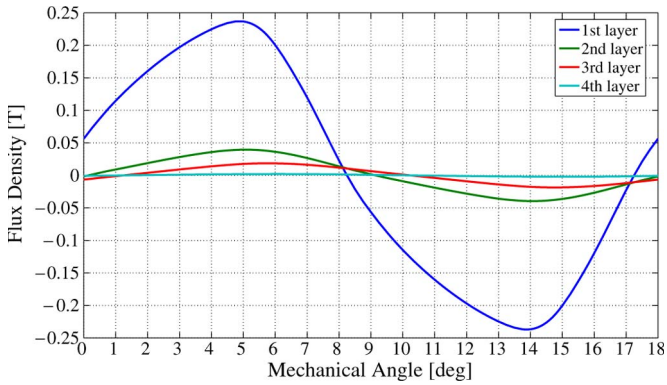

Fig. 18. Region (layer) radial-flux density variation in a stator coil side of a 40-pole 30-slot machine with open stator slots, versus rotor position.

An example of the region radial-flux density variations in a coil side is shown in Fig. 18. The first-layer plot in Fig. 18 is the flux density variation in the region closest to the air gap, while the fourth-layer plot is the flux density in the region farthest from the air gap. A discrete Fourier transform is applied to the calculated flux density information to determine the frequency and amplitude components of the flux density in a region. It is important to note that this method takes all sources of flux pulsations into account. The principle of superposition is then used to include the various frequency components in the loss calculation.

The different frequency losses of the optimum designed PM hub machines with equal active volumes were calculated, and it can be concluded from these results that the rotor iron losses are significant compared to the stator iron losses. Furthermore, PM machines with low winding factors and low lcm values have higher frequency losses than machines with good winding factors and higher lcm values. PM machines with wide open stator slots also have higher losses than machines with semiclosed stator slots.

The equations used to calculate the various frequency loss components of (5) are given in this Appendix.

A. Iron Losses

An improved iron loss formula is used in [28] that includes an excess specific loss component p_{exc} as

$$\begin{aligned} p_c &= p_h + p_e + p_{\text{exc}} \\ &= k_h f B^{\alpha} + k_e f^2 B^2 + k_{\text{exc}} f^{1.5} B^{1.5} \end{aligned} \tag{6}$$

where k_{exc} is the excess loss constant while k_h and k_e are the respective hysteresis and eddy current loss constants. These constants are calculated for the M19 fully processed N–O Si-Fe gauge-29 (0.35 mm) sheet steel.

B. Eddy Current Losses

If a conductor is exposed to an alternating magnetic field, the eddy current losses induced in that conductor can be calculated, as done in [29] and given by (8). The eddy current loss in the magnets is estimated by using (9), an equation given in [30] that calculates the instantaneous magnet loss density in the magnets.

C. Frequency Harmonic Loss Calculation

The method used to calculate the total frequency losses is explained in this Appendix. As explained, the principle of superposition is used to include the various frequency components in the loss calculation. Hence, if the number of regions is n and the number of harmonic orders considered is v, then the iron losses P_c can be calculated from (6) as

$$P_c = \sum_{j=1}^{n} \left(m_j \sum_{i=1}^{v} k_h f_{ij} B_{ij}^{\alpha} + k_e f_{ij}^2 B_{ij}^2 + k_{\text{exc}} f_{ij}^{1.5} B_{ij}^{1.5} \right) \tag{7}$$

where m_j is the mass of region j and f_{ij} and B_{ij} are the frequency and the flux density amplitude of harmonic order i of region j, respectively.

Similarly, the eddy current losses in the stator conductors are calculated from

$$P_s = \sum_{j=1}^{n} \left(n_{cj} \sum_{i=1}^{v} \frac{\pi^3 l d^4 B_{ij}^2 f_{ij}^2}{8\rho} \right) \tag{8}$$

where n_{cj} is the number of stator conductors in region j. For the low-voltage machines in this work, a copper wire with a diameter of 2 mm is used. The losses could be reduced by using bundles of thinner wire. The eddy current losses in the PMs are estimated as

$$P_m = \sum_{j=1}^{n} \left(Vol_j \sum_{i=1}^{v} \frac{\pi^2 b_j^2 f_{ij}^2 B_{ij}^2}{6\rho} \right) \tag{9}$$

where Vol_j is the volume of region j in the magnet, b_j is the magnet width, and ρ is the resistivity of the magnet material.

REFERENCES

[1] J. Malan and M. J. Kamper, "Performance of a hybrid electric vehicle using reluctance synchronous machine technology," *IEEE Trans. Ind. Appl.*, vol. 37, no. 5, pp. 1319–1324, Sep./Oct. 2001.

[2] J. P. Trovao, P. G. Pereirinha, and F. J. T. E. Ferreira, "Comparative study of different electric machines in the powertrain of a small electric vehicle," in *Proc. 18th Int. Conf. Elect. Mach.*, Vilamoura, Portugal, Sep. 2008, pp. 1–6.

[3] K. T. Chau, C. C. Chan, and L. Chunhua, "Overview of permanent-magnet brushless drives for electric and hybrid electric vehicles," *IEEE Trans. Ind. Electron.*, vol. 55, no. 6, pp. 2246–2257, Jun. 2008.

[4] N. Mutoh, T. Kazama, and K. Takita, "Driving characteristics of an electric vehicle system with independently driven front and rear wheels," *IEEE Trans. Ind. Electron.*, vol. 53, no. 3, pp. 803–813, Jun. 2006.

[5] L. Chunhua, K. T. Chau, and J. Z. Jiang, "A permanent-magnet hybrid brushless integrated starter-generator for hybrid electric vehicles," *IEEE Trans. Ind. Electron.*, vol. 57, no. 12, pp. 4055–4064, Dec. 2010.

[6] K. I. Laskaris and A. G. Kladas, "Internal permanent magnet motor design for electric vehicle drive," *IEEE Trans. Ind. Electron.*, vol. 57, no. 1, pp. 138–145, Jan. 2010.

[7] D. J. van Schalkwyk and M. J. Kamper, "Effect of hub motor mass on stability and comfort of electric vehicles," in *Proc. IEEE Veh. Power Propulsion Conf.*, Sep. 2006, pp. 1–6.

[8] J. Larminie and J. Lowry, "Electric vehicle modeling," in *Electric Vehicle Technology Explained*. West Sussex, U.K.: Wiley, 2003, pp. 183–212.

[9] J. Cros, P. Viarouge, and C. Gelinas, "Design of PM brushless motors using iron-resin composites for automotive applications," in *Conf. Rec. IEEE IAS Annu. Meeting*, Oct. 1998, vol. 1, pp. 5–11.

[10] A. G. Jack, B. C. Mecrow, P. G. Dickinson, D. Stephenson, J. S. Burdess, N. Fawcett, and J. T. Evans, "Permanent-magnet machines with powdered iron cores and prepressed windings," *IEEE Trans. Ind. Appl.*, vol. 36, no. 4, pp. 1077–1084, Jul./Aug. 2000.

[11] A. M. EL-Refaie, "Fractional-slot concentrated-windings synchronous permanent magnet machines: Opportunities and challenges," *IEEE Trans. Ind. Electron.*, vol. 57, no. 1, pp. 107–121, Jan. 2010.
[12] N. Bianchi and S. Bolognani, "Design techniques for reducing the cogging torque in surface-mounted PM motors," *IEEE Trans. Ind. Appl.*, vol. 38, no. 5, pp. 1259–1265, Sep./Oct. 2002.
[13] F. Libert and J. Soulard, "Investigation on pole–slot combinations for permanent-magnet machines with concentrated windings," in *Proc. 16th Int. Conf. Elect. Mach.*, Cracow, Poland, Sep. 2004.
[14] M. Yoneda, M. Shoji, Y. Kim, and H. Dohmeki, "Novel selection of the slot/pole ratio of the PMSM for auxiliary automobile," in *Conf. Rec. IEEE IAS Annu. Meeting*, Oct. 2006, vol. 1, pp. 8–13.
[15] J. Cros and P. Viarouge, "Synthesis of high-performance PM motors with concentrated windings," *IEEE Power Eng. Rev.*, vol. 22, no. 4, p. 74, Apr. 2002.
[16] Z. Q. Zhu, D. Ishak, D. Howe, and C. Jintao, "Unbalanced magnetic forces in permanent-magnet brushless machines with diametrically asymmetric phase windings," *IEEE Trans. Ind. Appl.*, vol. 43, no. 6, pp. 1544–1553, Nov. 2007.
[17] F. Magnussen and H. Lendenmann, "Parasitic effects in PM machines with concentrated windings," *IEEE Trans. Ind. Appl.*, vol. 43, no. 5, pp. 1223–1232, Sep. 2007.
[18] C. C. Hwang, M. H. Wu, and S. P. Cheng, "Influence of pole and slot combinations on cogging torque in fractional slot PM motors," *J. Magn. Magn. Mater.*, vol. 304, no. 1, pp. e430–e432, Sep. 2006.
[19] N. Bianchi, M. Dai Prè, L. Alberti, and E. Fornasiero, "Rotor losses in fractional-slot PM machines," in *Theory and Design of Fractional-Slot PM Machines*, 1st ed., *IEEE Industry Applications Society: Tutorial Course Notes*. Padova, Italy: CLEUP, 2007, pp. 157–173.
[20] M. J. Kamper, A. J. Rix, D. A. Wills, and R.-J. Wang, "Formulation, finite-element modeling and winding factors of non-overlap winding permanent magnet machines," in *Proc. 18th Int. Conf. Elect. Mach.*, Vilamoura, Portugal, Sep. 2008, pp. 1–5.
[21] S. E. Skaar, O. Krovel, and R. Nilsen, "Distribution, coil-span and winding factors for PM machines with concentrated windings," presented at the 17th Int. Conf. Electrical Machines, Chania, Greece, Sep. 2006, Paper 346.
[22] M. V. Cistelecan and M. Popescu, "Study of the number of slots/pole combinations for low speed permanent magnet synchronous generators," in *Proc. IEEE Elect. Mach. Drives Conf.*, May 2007, vol. 2, pp. 1616–1620.
[23] F. Magnussen and H. Lendenmann, "Parasitic effects in PM machines with concentrated windings," *IEEE Trans. Ind. Appl.*, vol. 43, no. 5, pp. 1223–1232, Sep./Oct. 2007.
[24] Y. Perriard, P. Ragot, and M. Markovic, "Brushless DC motor optimization process—Choice between standard or straight tooth shape," in *Conf. Rec. IEEE IAS Annu. Meeting*, Oct. 2006, vol. 4, pp. 1898–1904.
[25] M. J. D. Powell, "An efficient method for finding the minimum of a function of several variables without calculating derivatives," *Comput. J.*, vol. 7, no. 2, pp. 155–162, 1964.
[26] A. J. Rix, M. J. Kamper, and R.-J. Wang, "Design and performance evaluation of concentrated coil permanent magnet machines for in-wheel drives," in *Proc. IEEE Elect. Mach. Drives Conf.*, May 2007, pp. 770–775.
[27] H. W. de Kock, A. J. Rix, and M. J. Kamper, "Optimal torque control of synchronous machines based on finite-element analysis," *IEEE Trans. Ind. Electron.*, vol. 57, no. 1, pp. 413–419, Jan. 2010.
[28] F. Deng, "An improved iron loss estimation for permanent magnet brushless machines," *IEEE Trans. Energy Convers.*, vol. 14, no. 4, pp. 1391–1395, Dec. 1999.
[29] R.-J. Wang and M. J. Kamper, "Calculation of eddy current loss in axial field permanent-magnet machine with coreless stator," *IEEE Trans. Energy Convers.*, vol. 19, no. 3, pp. 532–538, Sep. 2004.
[30] H. Polinder and M. J. Hoeijmakers, "Eddy-current losses in the segmented surface-mounted magnets of a PM machine," *Proc. Inst. Elect. Eng.—Elect. Power Appl.*, vol. 146, no. 3, pp. 261–266, May 1999.

Arnold J. Rix (M'07) received the B.Eng. and Ph.D. (Eng.) degrees from Stellenbosch University, Stellenbosch, South Africa, in 2004 and 2011, respectively. The focus of his Ph.D. study was on the design, comparison, and evaluation of nonoverlap-winding hub drives.

He was with Stellenbosch University, where he presented an undergraduate practical course on electrical machines and drives. He is currently a Product Engineer with Isivunguvungu Wind Energy Converter (Pty) Ltd., Cape Town, South Africa, where he focuses on large wind turbines in the renewable energy industry.

Maarten J. Kamper (M'95–SM'08) received the M.Sc. (Eng.) and Ph.D. (Eng.) degrees from Stellenbosch University, Stellenbosch, South Africa, in 1987 and 1996, respectively.

Since 1989, he has been a Member of the academic staff with the Department of Electrical and Electronic Engineering, Stellenbosch University, where he is currently a Professor of electrical machines and drives. His research interests include computer-aided design and control of reluctance, permanent-magnet, and induction machine drives.

Prof. Kamper is a South African National Research Foundation Supported Scientist and a Registered Professional Engineer in South Africa.